EARTHQUAKE ENGINEERING AND STRUCTURAL DYNAMICS
Earthquake Engng. Struct. Dyn. **28**, 633–653 (1999)

NON-LINEAR SEISMIC ANALYSIS OF BASE-ISOLATED RC FRAME STRUCTURES

C. CECCOLI, C. MAZZOTTI AND M. SAVOIA*
Distart-Structural Engineering, University of Bologna, Viale Risorgimento 2, 40136 Bologna, Italy

SUMMARY

In this paper, seismic analysis of plane RC frame structures with High Damping Rubber Bearings (HDRBs) base-isolation systems is performed in the non linear range. For RC members, a modified version of hysteretic Park model is used. For HDRB isolators, a new hysteretic model is presented, which is able to accurately predict the mechanical response in the large strain range. The dynamic equilibrium equations are solved making use, at each time step, of a block iterative Newton–Raphson scheme: the frame is divided into superelements (beams and columns) with master nodes at the extremities and internal local nodes for the computation of relations between end moments and relative rotations at superelement extremities. The effectiveness of HDRB base-isolation systems to reduce inelastic deformations in the RC superstructures is investigated through some numerical examples. Copyright © 1999 John Wiley & Sons, Ltd.

KEY WORDS: RC frames; base isolation; hysteretic models; HDRB model; energy dissipation

1. INTRODUCTION

Base isolation with High-Damping Rubber Bearings (HDRBs) is today considered an important strategy for the protection of buildings of strategic or monumental interest subject to earthquakes[1]. Well-designed base-isolation systems allow for damage reduction in structural elements for strong ground motions and for protection of sensitive equipment for moderate earthquakes. Numerical studies reported in the literature show that comparable performances of base-isolated RC frames can be achieved designing to between 25 and 50 per cent of lateral forces required to design conventional (fixed-base) frames.[2] Hence, the cost of base-isolation system can be balanced by reduction of costs of the superstructure.

Following the usual protection strategy, making use of elastomeric bearings between superstructure and foundation, the fundamental frequency of the building is set lower than the dominant frequency range of input earthquake. Nevertheless, many recent studies showed that low stiffness of base-isolation systems could cause unacceptably large displacements of ground floor of the building for low-frequency ground motions or near-field excitations. The use of

* Correspondence to: M. Savoia, Distart-Structural Engineering, Faculty of Engineering, University of Bologna, Viale Risorgimento 2, 40136 Bologna, Italy. E-mail: marco.savoia@mail.ing.unibo.it

Contract/grant sponsor: MURST
Contract/grant sponsor: COSMES

CCC 0098–8847/99/060633–21$17·50

Received 5 February 1998
Revised 29 November 1998

HDRBs, assuring high-energy dissipation when working out of linear range, is then highly recommended.[3,4]

The seismic response of base-isolated RC structures is usually investigated following two alternative ways, i.e. making use of full non-linear analyses[5–7] or linearized techniques based on equivalent hysteretic damping factors.[8,9] In the case of highly non-linear isolators, the first way is usually recommended. Moreover, the use of hysteretic models for both superstructure and isolators allows for the estimate of damage reduction with respect to fixed-base structure, essential for an efficient design of base-isolation systems.

For RC members, hysteretic models are typically classified into local, semi-local (or fibre) and global models, depending on the nature of variables (local or cross-sectional) used to describe stresses and displacements (see, for instance, the state-of-art report published by CEB[10] and recent papers[11,12]). For the study of real-size structures, the reduced computational effort makes global models particularly attractive for non-linear dynamic analyses. The constitutive model is defined in terms of generalized co-ordinates and is usually based on experimental observations.

For HDRBs, several experimental tests showed strong non-linearities in shear force-displacement constitutive law, with significant hardening behaviour at large strains due to geometrical effects. Hence, classical bilinear and Ramberg–Osgood analytical models are often inadequate. More complex constitutive models have been recently proposed.[5,7]

In the present paper, the numerical analysis of plane RC structures with HDRB base-isolation systems and subject to seismic excitation is performed. The hysteretic model adopted for RC members (Section 2) basically operates on a trilinear skeleton curve for monotonic loading. The piecewise-linear incremental relations describing unloading and reloading conditions are mainly based on the Park model,[13] including stiffness deterioration caused by concrete cracking and reduction of hysteresis loop due to pinching effect. Modifications are included to describe strength degradation for severe plastic deformations. The influence on hysteretic damping ratio of parameters governing pinching effect and strength degradation is investigated in detail.

The HDRB isolators are modelled as shear-deformable elements in Section 3. The proposed hysteretic model is based on a third-order polynomial curve for monotonic loading and different rules for loading and unloading in the ranges of small and large strains. The model is able to accurately reproduce the hysteresis loops obtained from quasi-static experimental tests on HDRBs recently performed at the Ismes Dynamic Laboratory (Bergamo, Italy).

The non-linear seismic analysis of base-isolated structures is performed in the time domain. The equations of motion are integrated making use of the block-iterative Newton–Raphson algorithm (Section 4). The structure is divided into superelements, corresponding to beams and columns, with master nodes at their extremities and local nodes to compute, at intermediate sections, the non-linear relation between moments and corresponding relative rotations at the RC superelement extremities. For each time step, the iterative solution of equilibrium equations at the superelement level and at the structure level is performed. In the numerical simulations presented in Section 5, the effectiveness of base-isolation systems with HDRBs is investigated. The behaviours of conventional and base-isolated RC frames subject to different earthquake ground motions are compared. The dissipated energy in RC members during hysteresis loops is computed, so evaluating the potential damage of superstructure. It is shown that, in some cases, setting the frequency of the base-isolated building lower than the dominate frequency range of the earthquake motion is not sufficient for an efficient design of base-protection systems.

This study represents the starting point for future studies on effectiveness of base-isolation systems for building aseismic protection. In this context, it is to be remembered the importance

that recent studies reserved to near-field thrust-fault generated earthquakes,[14–16] characterized by large-amplitude velocity pulses and large ground displacements. These earthquakes can be very dangerous for base-isolated structures, requiring drift demands far exceeding the present code recommendations.[15]

2. THE HYSTERETIC MODEL FOR RC MEMBERS

A hysteretic model has been developed for the RC beam/column elements. The incremental moment–curvature constitutive relation for the cross-section follows a set of different rules for loading and unloading conditions. Particular attention has been devoted to describe peculiar situations that may occur when the excitation is irregular (as in the case of earthquake ground motion), such as reloading during unloading branches, etc.

The model adopted is based on the Park *et al.* model,[13] including stiffness degradation during unloading and reduction of size of hysteretic loop due to pinching effect. Some modifications have been included to describe reloading curves and strength degradation due to concrete cracking and concrete/steel bond deterioration in the range of severe plastic deformations.

The hysteretic model is based on a trilinear curve for monotonic loading response with two breakpoints, corresponding to initial concrete cracking (χ_c, M_c) and initial yielding of steel reinforcement (χ_y, M_y). Post-ultimate failure branch is not considered, i.e. no curvature limit is considered during steel post-yielding branch. The effect of axial force is not presently considered. Nevertheless, it can be easily included in approximate form by considering a modified yielding moment due to axial force.[17,11]

The most important phenomena included in the present model are briefly summarized in the following (see Figure 1):

(1) *Stiffness degradation* (Figure 1(a)): Unloading direction from post-cracking situations intersects the uncracked branch at an ordinate equal to α times the yielding moment in the opposite direction (Point *A*). This direction is maintained until the situation of null bending moment is reached (Point *N*). Loading in the opposite direction follows two different ways if, alternatively, previous loading reached post-cracking branch or steel post-yielding branch. Reloading branch points at the maximum curvature χ_{max} previously reached.

(2) *Loading after concrete post-cracking*: according to Costa and Costa,[18] loading branch after null moment situation points at the maximum curvature χ_{max} previously reached in that sense (positive or negative bending moment). If that value was lower than initial cracking curvature, reloading branch points at initial cracking situation.

(3) *Loading after steel post-yielding* (*pinching effect*) (Figure 1(b)): Loading branch points initially at the intersection between unloading branch from the maximum deformation (χ_{max}) and a line at $\gamma M_y = \text{const.}$ (Point *R*), until the curvature χ_{cl} is reached, corresponding to the intersection between unloading and null moment ordinate (crack closing co-ordinate). Then, loading branch points at the maximum previous curvature reached in that loading direction. Lower values of parameter γ determine higher pinching effects.

(4) *Strength degradation* (Figure 1(c)): Strength degradation occurs if curvature $\chi_{max} > \beta\chi_y$ has been reached during previous cycles ($\beta > 1$); in this case, reloading branch points at the intersection between a line with negative slope equal to δ times the stiffness of post-yielding branch and the χ_{max} abscissa (Point *S*). When the curvature χ_{max} is reached, loading continues

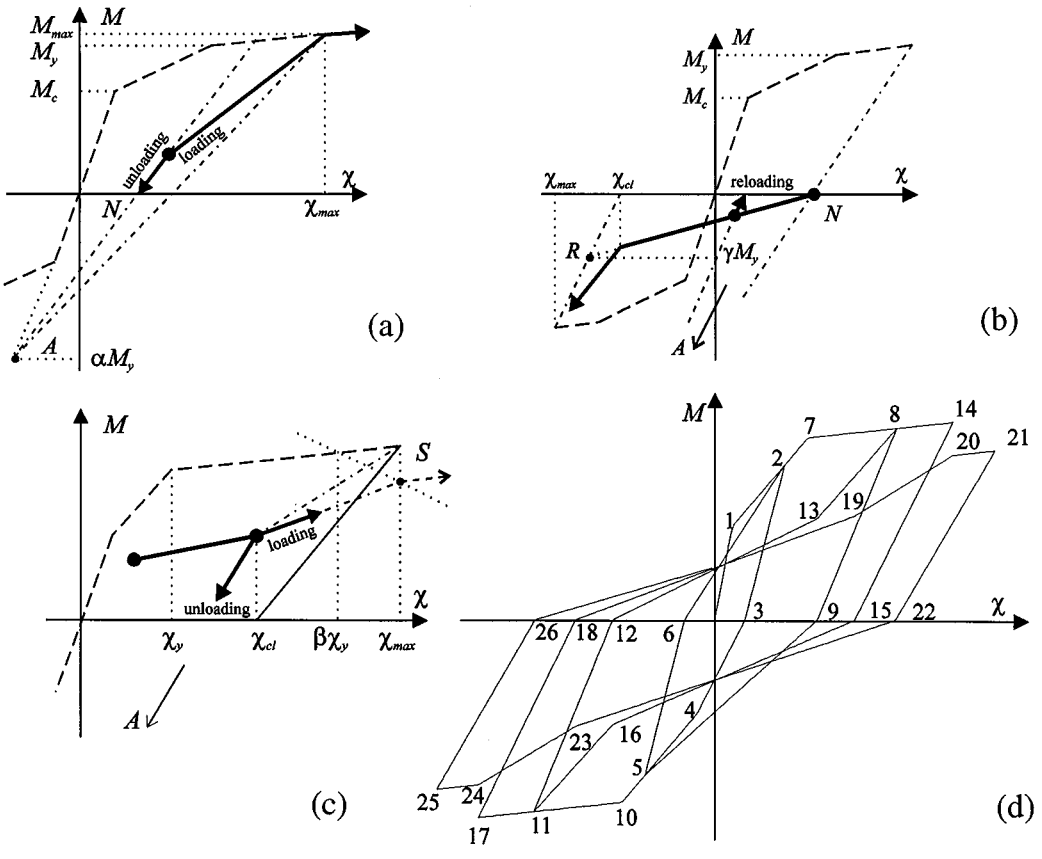

Figure 1. Hysteretic model for RC members: (a) stiffness degradation during unloading; (b) pinching effect; (c) strength degradation; (d) hysteretic loops for increasing maximum curvature

along a line parallel to the original monotonic curve. The technique used to take strength degradation into account is similar to those proposed in References 11 and 18 and simpler than that used in Reference 12 where a curvilinear degradation path is adopted, depending on a damage index.

The rules adopted in the present hysteretic model are summarized in Figure 1(d), showing four hysteresis loops for increasing values of maximum curvature:

1° loop (1–6): concrete cracking ($\chi_c < [\chi_2, \chi_5] < \chi_y$);
2° loop (6–12): steel yielding, stiffness degradation during unloading ($\chi_y < [\chi_8, \chi_{11}]] < \beta\chi_y$);
3° loop (12–18): pinching effect ($\chi_c < [\chi_{14}, \chi_{17}] < \beta\chi_y$);
4° loop (18–26): strength degradation ($\beta\chi_y < [\chi_{21}, \chi_{25}]$).

The hysteretic behaviour of the cross-section is strongly affected by the values assumed by parameters α, β, γ, δ, depending on geometrical and mechanical properties of the cross-section.

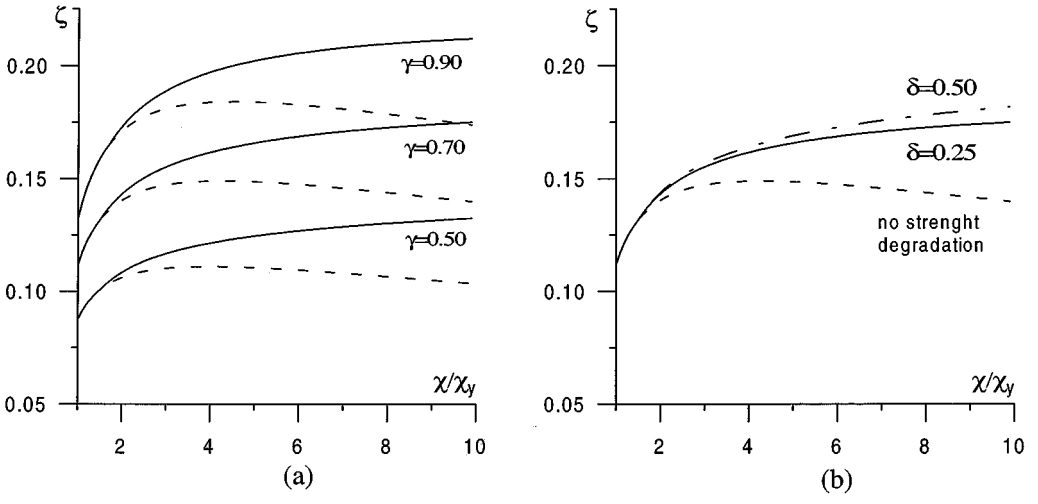

Figure 2. Hysteretic damping ratio for RC cross-sections (a) versus pinching parameter γ ((—) strength degradation included; (- - -) strength degradation excluded; $\delta = 1$ is adopted) and (b) versus parameter δ governing the strength degradation effect

The choice of numerical values must be guided by experimental investigations. For instance, the values $\alpha = 2$, $\gamma = 0{\cdot}7$, $\beta = 3{\cdot}5$ are suggested in References 13 and 19 for given cross-sections.

For a RC cross-section with size 300 mm × 400 mm and symmetric steel reinforcement $(3 + 3)\phi 12$, the influences on hysteretic damping ratio[20] of pinching effect and strength degradation are investigated. The mechanical characteristics adopted for concrete and steel are: $E_c = 31977$ MPa, $f'_c = 24{\cdot}9$ MPa, $f'_t = 4{\cdot}8$ MPa, $E_s = 210\,000$ MPa, $f_y = 380$ MPa. Concrete cracking and steel yielding conditions are defined according to CEB-FIP Model Code[21]. Pinching effect is governed by parameter γ, whereas strength degradation depends on β and δ. In the present model, β is determined so as to obtain a smooth transition of hysteretic damping ratio from the undegraded condition to the damaged state. In Figure 2(a), different values of γ are considered. Solid and dashed lines denote the hysteretic damping ratio with strength degradation included and excluded, respectively. The figure shows that strength degradation must be taken into account in order to have the hysteretic damping ratio monotonically increasing with curvature amplitude, as is predicted by experimental investigations.[22] The same figure outlines the importance of the value adopted for the pinching parameter γ: for instance, at $\chi/\chi_y = 10$ the hysteretic damping ratio for $\gamma = 0{\cdot}9$ is about 60 per cent greater than for $\gamma = 0{\cdot}5$. Finally, Figure 2(b) shows that the damping ratio is moderately sensitive to variations of parameter δ, governing the slope of line where reloading branch points when strength degradation occurs.

3. THE HYSTERETIC MODEL FOR RUBBER BEARINGS

A hysteretic model has been recently formulated by the authors for high-damping steel laminated rubber bearings (HDRBs).[5] The model has been improved here and used to model the hysteretic behaviour of a set of HDRBs subject to quasi-static experimental tests at the Ismes Dynamic

Laboratory (Bergamo, Italy). The tests confirmed that the hysteretic behaviour strongly depends on geometrical and mechanical characteristics of the isolator (rubber chemical composition, isolator shape factor, ratio between heights of rubber layers and steel laminae). Moreover, significant hardening phenomena occur for isolators working in the large strain range. Consequently, a mechanical model must be sufficiently 'flexible' in order to attain a reasonable level of generality. Since the solution procedure adopted for seismic analysis is a numerical integration of non-linear dynamic equations (see Section 4), incremental hysteretic models based on higher-order curves for loading and unloading can be adopted without significant additional computational effort with respect to classical bilinear approximations.

The proposed hysteretic model is based on a polynomial monotonic loading curve obtained through interpolation of experimental results. The hardening behaviour occurring for large strains ($\gamma > 100$ per cent) due to large displacement phenomenon can then be easily included. Different rules are adopted to describe loading and unloading branches for small and large strains. Vertical deformability is neglected, due to the presence of steel laminae assuring high stiffness in the vertical direction. The main features of the model are described below (see Figure 3):

(a) *Linear range*: Linear behaviour is considered for the first branch from the virgin state, until the hysteretic curve of monotonic loading is reached. G_1 denotes the shear stiffness in the linear branch.
(b) *Monotonic loading curve*: The monotonic loading curve is given by a complete third-order polynomial obtained through interpolation of experimental results. T_0 and G_0 denote shear resultant and stiffness (slope of loading curve) corresponding to null shear strain. These parameters are considered independent of the amplitude of hysteresis loops and adopted as basic parameters for the hysteretic model.
(c) Two different unloading curves are used for small ($\gamma < \bar{\gamma}$) and large ($\gamma > \bar{\gamma}$) shear strains:
  (1) *Unloading in the small strain range* is given by an exponential curve written in terms of local coordinates (t, Γ) as (see Figure 3):

$$t = f_1(\Gamma) = a\Gamma + b\exp(-c\Gamma) \tag{1}$$

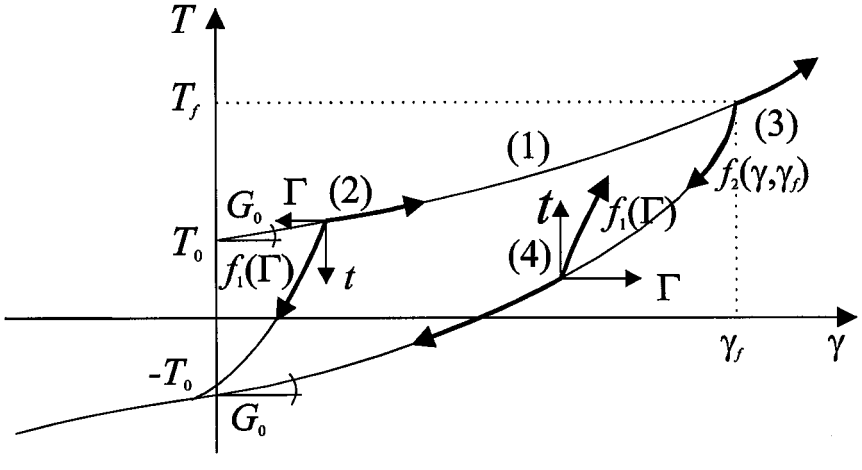

Figure 3. Hysteretic model for HDRBs: (1) monotonic loading curve; (2) unloading from small strains; (3) unloading from large strains; (4) reloading during unloading; T_0, G_0: shear and tangent stiffness at null shear strain

with the origin of the co-ordinate system located in the point of initial unloading. Parameters a and b are obtained by setting the stiffness of initial unloading equal to the elastic stiffness G_1 and the asymptotic value for large Γ equal to G_0. The third parameter, c, is obtained through interpolation of experimental data. Unloading branch stops when the monotonic loading curve in the opposite direction is reached.

(2) *Unloading in the large strain range* follows a three-term polynomial–exponential curve:

$$T = f_2(\gamma, \gamma_f) = -T_0 + a\gamma - b\gamma(1 - \exp[-c(\gamma - \gamma_f)]) \tag{2}$$

Parameters a, b are obtained by imposing $T_f = T(\gamma_f)$, with γ_f, T_f being the shear strain and shear resultant of initial unloading, so obtaining

$$a = \frac{T_f - T_0}{\gamma_f}, \qquad b = \frac{a - G_0}{1 - \exp(-c\gamma_f)} \tag{3}$$

Moreover, c is given by an empirical (polynomial) function, such that tangent stiffness of initial unloading is close to the elastic stiffness G_1.

(d) *Reloading branch starting from unloading curve* follows, for both small and large strains, a curve analogous to the unloading branch from small strains. The curve is given by the same polynomial law of equation (1) in terms of local co-ordinates $t = f_1(\Gamma)$, but in the opposite direction (see Figure 3).

A set of quasi-static experimental tests has been performed at Ismes Dynamic Laboratory to determine the hysteresis loops of HDRBs subject to constant vertical loads and increasing maximum shear strains. The HDRB diameter and thickness of rubber were 150 and 28 mm, respectively. The isolators were designed for a 1/3-scale RC building model subject to shaking-table dynamic tests (see Section 5). The value $\bar{\gamma} = 40$ per cent is adopted to differentiate small strain from large strain behaviours. The experimental results for a vertical load equal to 76 kN are reported in Figure 4(a), and the numerical simulation with the proposed model is depicted in Figure 4(b). A substantial agreement between experimental and numerical results is reached. It is very good in the range of large strains, so allowing for a correct evaluation of hysteretic damping behavior for strong base motions. The agreement is rather worse for small strain cycles ($\bar{\gamma} < 40$ per cent), leading to overestimate the damping in this range. To improve the model, more complex rules for the unloading branch must be adopted.

4. THE NUMERICAL PROCEDURE

The hysteretic models for RC members and HDRBs described in the previous sections have been used to perform the non-linear analysis of base-isolated frame structures subject to seismic excitation. For the numerical integration of dynamic equilibrium equations, a block iterative Newton–Raphson method has been developed, whose guidelines are described in this section.

4.1. Time step-by-step integration

The response of a m.d.o.f subject to seismic excitation can be obtained through stepping-time integration of the system of differential equations:

$$\mathbf{M}\ddot{\mathbf{x}}(t) + \mathbf{C}\dot{\mathbf{x}}(t) + \mathbf{K}(\mathbf{x}(t))\mathbf{x}(t) = -\mathbf{M}\mathbf{I}\ddot{\mathbf{x}}_g(t) \tag{4}$$

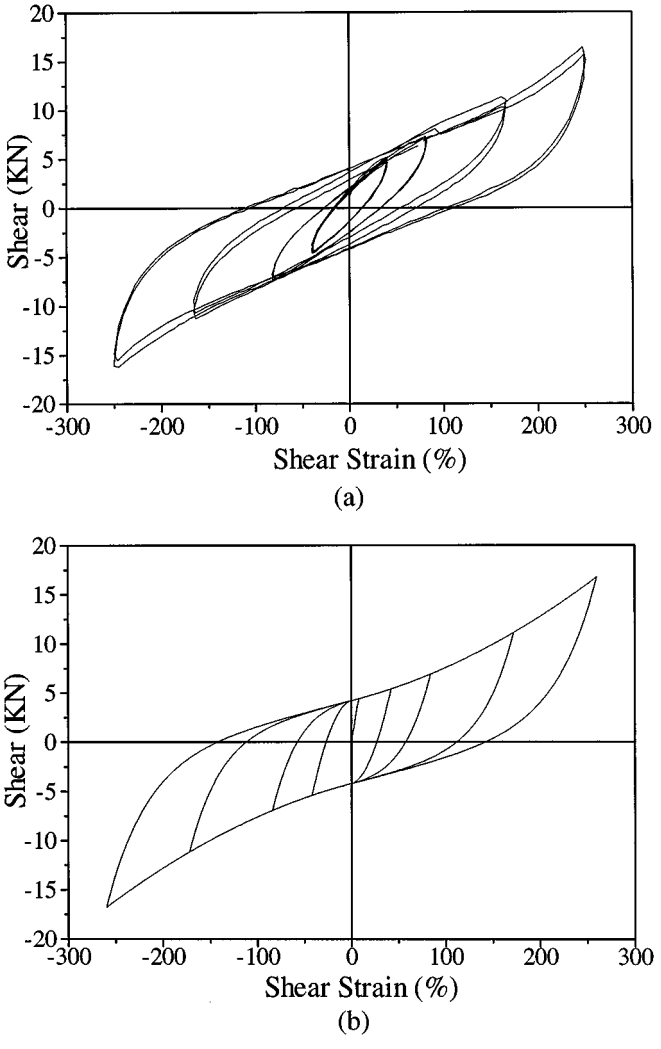

Figure 4. Hysteresis loops at increasing values of maximum shear strains for a HDRB subject to 76 kN vertical load: (a) Experimental results; (b) Numerical simulation with the proposed hysteretic model

where **M**, **C** and **K** denote mass, viscous damping and stiffness matrices, respectively, $\mathbf{x}(t)$, $\dot{\mathbf{x}}(t)$ and $\ddot{\mathbf{x}}(t)$ are nodal displacements, velocities and accelerations, $\ddot{\mathbf{x}}_g(t)$ is the ground acceleration and **I** is the identity matrix. Matrices **M** and **C** are considered time independent, whereas $\mathbf{K}(\mathbf{x}(t))$ is a non-linear stiffness matrix defined according to incremental relations.

Making use of the classical Newmark step-by-step integration scheme, equation (4) can be rewritten, at the general nth time instant (i.e., at $t = n\Delta t$), in the form

$$\mathbf{M}\,\ddot{\mathbf{x}}_n + \mathbf{C}\,\dot{\mathbf{x}}_n + \mathbf{K}_n\mathbf{x}_n = -\mathbf{M}\mathbf{I}\,\ddot{\mathbf{x}}_{g,\,n} \tag{5}$$

If constant-average-acceleration method[23] is adopted, velocity and acceleration at time $t = (n + 1)\Delta t$ can be written as a function of quantities evaluated at the previous time instant, i.e. $\mathbf{x}_n, \dot{\mathbf{x}}_n, \ddot{\mathbf{x}}_n$ and of the unknown $\mathbf{x}_{n+1}$. Then, the dynamic equilibrium equation (4) at time $(n + 1)\,\Delta t$ can be written in the form of a system of algebraic equations

$$\mathbf{K}^*_{n+1}\,\mathbf{x}_{n+1} = \mathbf{f}^*_{n+1} \tag{6}$$

where

$$\mathbf{K}^*_{n+1} = \frac{4}{\Delta t^2}\,\mathbf{M} + \frac{2}{\Delta t}\,\mathbf{C} + \mathbf{K}_{n+1} \tag{7a}$$

$$\mathbf{f}^*_{n+1} = -\mathbf{M}\mathbf{I}\,\ddot{\mathbf{x}}_{g,n+1} + \mathbf{M}\left(\frac{4}{\Delta t^2}\mathbf{x}_n + \frac{2}{\Delta t}\dot{\mathbf{x}}_n + \ddot{\mathbf{x}}_n\right) + \mathbf{C}\left(\frac{2}{\Delta t}\mathbf{x}_n + \dot{\mathbf{x}}_n\right) \tag{7b}$$

Following a step-by-step time integration, the load vector $\mathbf{f}^*_{n+1}$ is known, depending on quantities evaluated at the previous (nth) time step and on prescribed ground acceleration, whereas the stiffness matrix $\mathbf{K}^*_{n+1}$ is unknown if the structural behaviour is non-linear. Making use of a modified Newton–Raphson iterative scheme, and denoting by $\mathbf{K}_{el}$ the initial (elastic) stiffness matrix, equation (6) is rewritten as

$$\mathbf{K}_{el}\,\mathbf{x}_{n+1} = \mathbf{p}^*_{n+1} \tag{8}$$

where the fictitious load vector is given by $\mathbf{p}^*_{n+1} = \mathbf{f}^*_{n+1} - (\mathbf{K}^*_{n+1} - \mathbf{K}_{el})\,\mathbf{x}_{n+1}$. At the first step, equation (8) is solved by setting $\mathbf{p}^*_{n+1} = \mathbf{f}^*_{n+1}$. = If the behaviour is not linear, i.e. $\mathbf{K}^*_{n+1} \neq \mathbf{K}_{el}$, the solution does not satisfy equilibrium equation (8), and the residual vector $\mathbf{r}_{n+1} = \mathbf{f}^*_{n+1} - \mathbf{p}^*_{n+1}$ is used as a new load vector. The iterative procedure is performed until the prescribed convergence is reached.

A significant improvement of convergence properties of the method has been obtained by adopting initial (elastic) and tangent stiffness matrices for RC structure and isolators, respectively. In fact, as will be shown in the numerical examples, moderately non-linear effects usually arise in RC superstructure when base isolation is present, whereas isolators may be subject to very high shear strain levels. Moreover, very few d.o.f's are necessary for the isolators: one d.o.f. only is required for planar structures with rigid ground floor slab (the same shear strain for all the isolators).

4.2. Master and local d.o.f.'s

The computational effort required for the solution of non-linear system (8) can be strongly reduced by adopting block iterative schemes. For instance, a block iterative technique has been used in Reference 24 to uncouple the motion equations of a frame structure from those of the base of isolation system.

In the present computational procedure, the structure is subdivided into a set of N superelements (i.e. single beams and columns), with M master nodes at their extremities (Figure 5). Hence, the displacement vector $\mathbf{x}_{n+1}$ is split into a set of subvectors: vector $\mathbf{A}$ contains the $3 \times M$ master d.o.f.'s (i.e. displacements and rotation at the superelement extremities), whereas, for $I = 1, \ldots, N$, $(\boldsymbol{\alpha}_I)^T = \{\boldsymbol{\alpha}^T_{I1}, \ldots, \boldsymbol{\alpha}^T_{Im}\}$ and $\boldsymbol{\alpha}^T_{Ij} = \{\boldsymbol{\alpha}^1_{Ij}, \boldsymbol{\alpha}^2_{Ij}\}$ are subvectors each collecting the m local d.o.f.'s of the Ith superelement. The non-linear algebraic system (6) can then be rewritten as (subscript $n + 1$

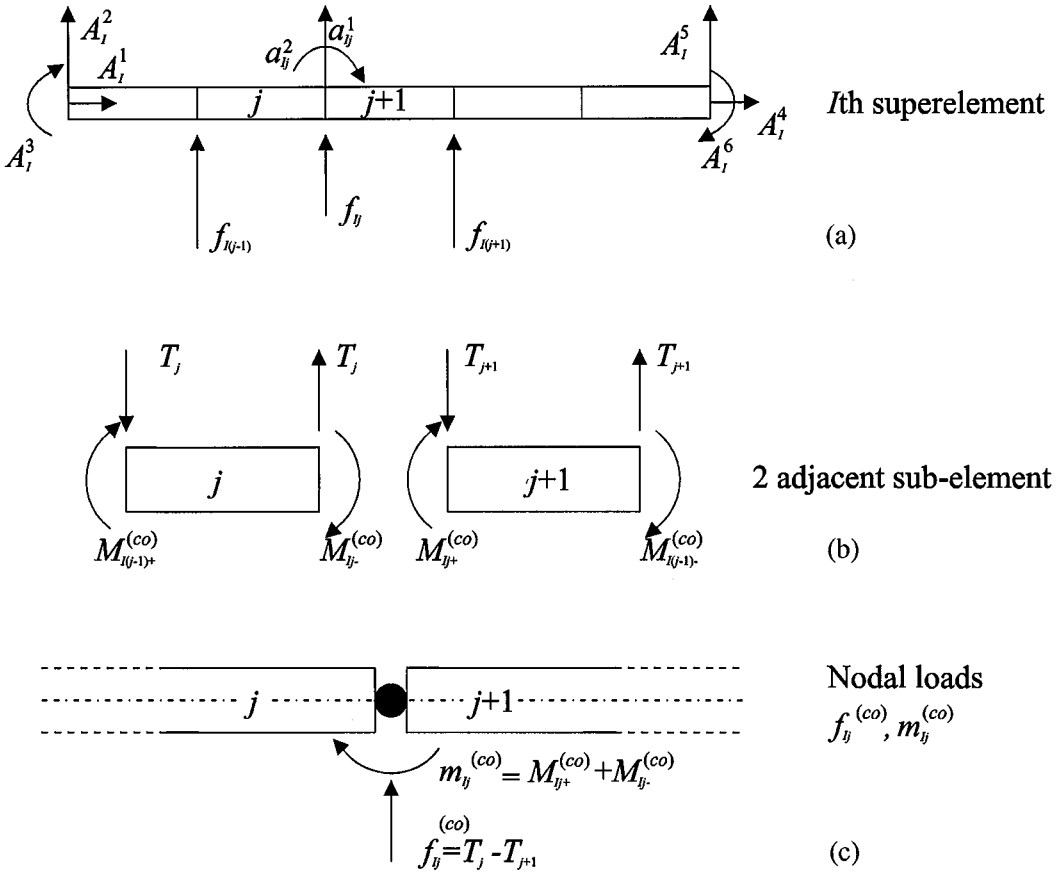

Figure 5. Block Newton–Raphson iterative scheme for the solution of dynamic equilibrium equations: (a) master and local d.o.f.'s; (b, c) notation adopted for subelement forces and nodal loads

and superscript * have been removed because unessential):

$$\begin{bmatrix} \mathbf{K}_{11} & \mathbf{0} & \mathbf{0} & \mathbf{K}_{1G} \\ \mathbf{0} & \cdots & \cdots & \cdots \\ \mathbf{0} & \cdots & \mathbf{K}_{NN} & \mathbf{K}_{NG} \\ \mathbf{K}_{G1} & \cdots & \mathbf{K}_{GN} & \mathbf{K}_{GG} \end{bmatrix} \begin{Bmatrix} \boldsymbol{\alpha}_1 \\ \cdots \\ \boldsymbol{\alpha}_N \\ \mathbf{A} \end{Bmatrix} = \begin{Bmatrix} \mathbf{f}_1 \\ \cdots \\ \mathbf{f}_N \\ \mathbf{F} \end{Bmatrix} \tag{9}$$

The solution of Ith local equilibrium equation of non-linear system (9) is

$$\boldsymbol{\alpha}_I = \mathbf{K}_{II}^{-1}(\mathbf{f}_I - \mathbf{K}_{IG}\mathbf{A}) \quad (I = 1, \ \ldots, N) \tag{10}$$

and substitution in the last equation of (9) gives

$$\mathbf{K}_{\mathrm{c}}\mathbf{A} = \mathbf{F}_{\mathrm{c}} \tag{11}$$

where

$$\mathbf{K}_{\mathrm{c}} = \mathbf{K}_{GG} - \sum_{I=1}^{N} \mathbf{K}_{GI}\,\mathbf{K}_{II}^{-1}\,\mathbf{K}_{IG}, \qquad \mathbf{F}_{\mathrm{c}} = \mathbf{F} - \sum_{I=1}^{N} \mathbf{K}_{GI}\,\mathbf{K}_{II}^{-1}\,\mathbf{f}_{I} \tag{12}$$

If the structural behaviour is linear, $\mathbf{K}_{\mathrm{c}}$ and $\mathbf{F}_{\mathrm{c}}$ coincide with the elastic matrix $\bar{\mathbf{K}}_{\mathrm{el}}$ and nodal load vector $\bar{\mathbf{F}}$ obtained through static condensation with respect to master d.o.f.'s $\mathbf{A}$'s. In the case of non-linear behaviour, system (9) is solved via Newton–Raphson method, with iterative solution of local and global equilibrium equations. At the first step, global and local d.o.f.'s are obtained, respectively, from the linear solution of equations (11) and (10), i.e. with elastic stiffness matrices substituting the current (non-linear) matrices:

$$\mathbf{A} = \bar{\mathbf{K}}_{\mathrm{el}}^{-1}\mathbf{F}_{\mathrm{c}}, \qquad \boldsymbol{\alpha}_I = \mathbf{K}_{\mathrm{el},II}^{-1}(\mathbf{f}_I - \mathbf{K}_{\mathrm{el},IG}\mathbf{A}) \tag{13}$$

With reference to the Ith-superelement, local displacement vectors $\boldsymbol{\alpha}_I$ ($I = 1, \ldots, N$) and master node displacements are used to compute bending moments $M_{I\mathrm{j}-}^{(\mathrm{el})}$, $M_{I\mathrm{j}+}^{(\mathrm{el})}$ and curvatures $\chi_{I\mathrm{j}-}$, $\chi_{I\mathrm{j}+}$ at the subelement extremities. Then, from incremental moment–curvature relations, the bending moments $M_{I\mathrm{j}-}^{(\mathrm{co})}$, $M_{I\mathrm{j}+}^{(\mathrm{co})}$ corresponding to $\chi_{I\mathrm{j}-}$, $\chi_{I\mathrm{j}+}$ are obtained. If $\forall I = 1, \ldots, N$, $\forall j = 1, \ldots, m$, $M_{I\mathrm{j}-}^{(\mathrm{co})} = M_{I\mathrm{j}-}^{(\mathrm{el})}$ and $M_{I\mathrm{j}+}^{(\mathrm{co})} = M_{I\mathrm{j}+}^{(\mathrm{el})}$, the behaviour is linear and equations (13) give the exact solution. On the contrary, if the bending moments are different, the node Ij is not equilibrated. The set of nodal loads and nodal bending moments in equilibrium with $M_{I\mathrm{j}-}^{(\mathrm{co})}$, $M_{I\mathrm{j}+}^{(\mathrm{co})}$ is

$$f_{I\mathrm{j}}^{(\mathrm{co})} = \frac{M_{I\mathrm{j}-}^{(\mathrm{co})} + M_{I(\mathrm{j}-1)+}^{(\mathrm{co})}}{\Delta l} - \frac{M_{I(\mathrm{j}+1)-}^{(\mathrm{co})} + M_{I\mathrm{j}+}^{(\mathrm{co})}}{\Delta l}, \qquad m_{I\mathrm{j}}^{(\mathrm{co})} = M_{I\mathrm{j}+}^{(\mathrm{co})} + M_{I\mathrm{j}-}^{(\mathrm{co})} \tag{14}$$

where Δl denotes the subelement length. Hence, the non-vanishing residual vector $\Delta\mathbf{r}_I = \mathbf{f}_I - \mathbf{f}_I^{(\mathrm{co})}$ is used as an additional load vector to obtain, from equation (13b) with $\mathbf{A} = \mathbf{0}$, an additional contribution for the local node displacement vector $\Delta\boldsymbol{\alpha}_I$

$$\Delta\boldsymbol{\alpha}_I = \mathbf{K}_{\mathrm{el},II}^{-1}\,\Delta\mathbf{r}_I \tag{15}$$

This local (i.e. at the element level) Newton–Raphson iterative scheme is performed until the prescribed accuracy is reached, i.e. $\Delta\mathbf{r}_I \approx \mathbf{0}$. Then, the values of internal actions at the superelement extremities give the nodal loads $\mathbf{F}^{(\mathrm{co})}$ for the master d.o.f.'s and the corresponding global residual load $\Delta\mathbf{R} = \mathbf{F}$–$\mathbf{F}^{(\mathrm{co})}$. The residual load vector is used as the starting point for a global (structure) Newton–Raphson iterative scheme based on equation (13a).

4.3. The viscous damping matrix

The linear viscous damping matrix $\mathbf{C}$ is obtained in the usual way,[25,26] i.e. by assigning a damping index ζ_{s} to S dominant vibration modes ($s = 1, \ldots, S$) of the structure, and evaluating the damping coefficients $D_{\mathrm{s}} = 2\zeta_{\mathrm{s}}\mathrm{M}_{\mathrm{s}}\omega_{\mathrm{s}}$ for the damping matrix written in terms of modal coordinates, with M_{s} and ω_{s} denoting modal mass and vibration frequency of nth mode. The viscous damping matrix is then obtained as

$$\mathbf{C} = \mathbf{M}\left(\sum_{s=1}^{S} \frac{2\xi_{\mathrm{s}}\omega_{\mathrm{s}}}{M_{\mathrm{s}}}\,\boldsymbol{\phi}_{\mathrm{s}}\boldsymbol{\phi}_{\mathrm{s}}^{\mathrm{T}}\right)\mathbf{M} \tag{16}$$

where ϕ_s is the sth eigenvector. In the numerical simulations presented in Section 5, a number S of vibration modes equal to the number of floors of the structure (the fundamental modes) has been retained to compute the viscous damping matrix, with damping index $\zeta_s = 0{\cdot}05$.

5. EFFECTIVENESS OF BASE-ISOLATION FOR REDUCING STRUCTURAL DAMAGE

In the presence of severe earthquake motions, base isolation usually allows for a significant reduction of damage of both structural and non-structural elements. The effectiveness of base isolation is studied here by evaluating the energy dissipated during the hysteretic loops in RC superstructure, strictly related to inelastic deformations and, consequently, to structural damage. Plastic strain energy is considered a fundamental parameter to define the ultimate limit state in many seismic damage models.[22,27–30] For the RC hysteretic behaviour described in Section 2, the values $\alpha = 2$, $\gamma = 0{\cdot}7$ and $\delta = 1$ are adopted.

5.1. *Two-storey RC frame structure under ground pulse-type excitation*

The two-storey shear-type frame of Figure 6 is subject to a pulse-type ground motion with sinusoidal law, duration $\Delta t = 0{\cdot}30$ s and variable acceleration peak amplitude ($a_g = 1$–$5\,\mathrm{m/s^2}$). This kind of excitation has been used to schematize strong near-source earthquakes, resulting in forward only (not-reversing) ground motions.[14] Both conventional and base-isolated structures are considered. The HDRBs considered for base isolation are the full-scale version of the 1/3-scale HDRBs whose hysteresis loops have been reported in Figure 4.

The dissipated energy in RC columns is reported in Figure 7. Dashed line denotes the energy dissipated by the isolators. Since dissipated energy is strictly related to potential structural damage, base isolation is shown to provide for a very effective protection of the superstructure. For instance, the behaviour of the conventional structure exceeds the linear range for

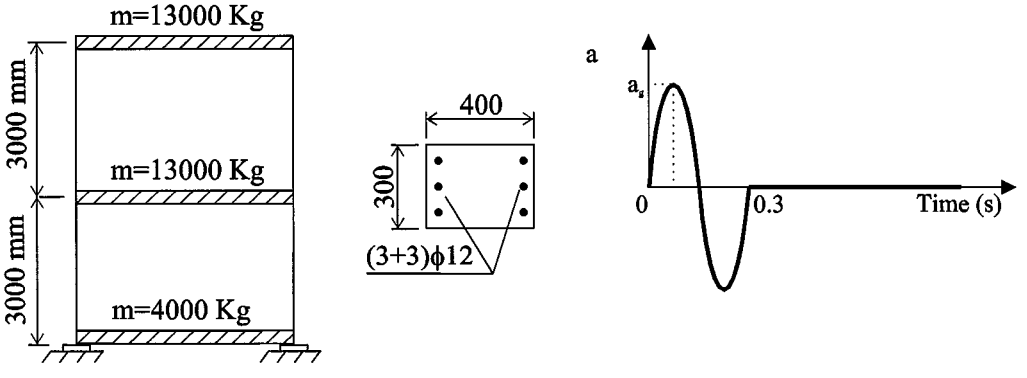

Figure 6. Base-isolated two-storey RC frame structures subject to ground pulse-type excitation

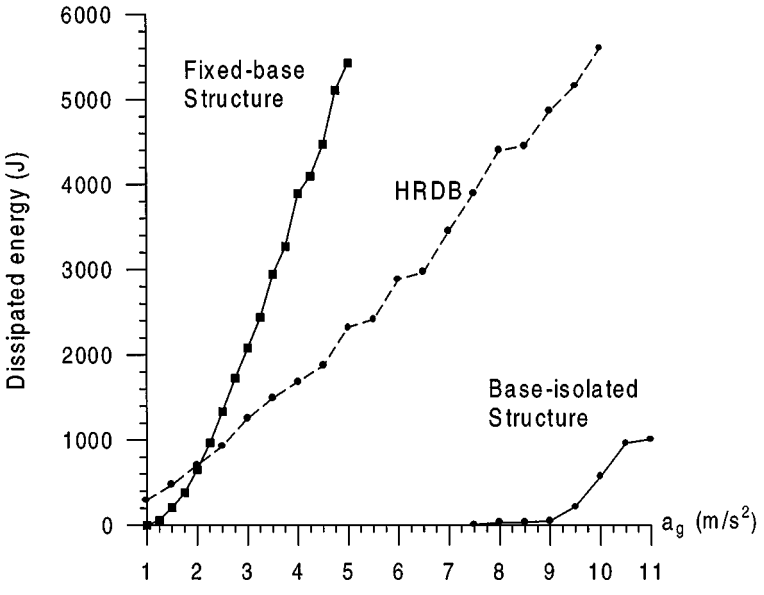

Figure 7. Hysteretic dissipated energy for conventional and base-isolated two-storey frame structures subject to ground pulse-type excitation versus maximum ground motion acceleration a_g

$a_g > 1{\cdot}25$ m/s^2, whereas that of base-isolated structure is linear until 7 m/s^2. Structural damage in columns of the fixed-base structure is confirmed by the significant horizontal drift of the first floor, equal to 2·6 mm for acceleration peak amplitude equal to 5 m/s^2 (with ratio between maximum curvature and curvature at steel yielding of column base, χ/χ_y, about 15), much higher than the 0·9 mm when base-isolation is present.

5.2. Frame structure under seismic excitation

The proposed non-linear model has been used to perform the numerical simulation of dynamic tests on a base-isolated framed RC structure. The object of the study is a base-isolated 1/3-scale model of a three-storey RC building subject to shaking-table tests in the framework of the research program 'Technologies for the Earthquake Protection of Buildings' financed by the COSMES group (Figure 8). The floors are squared with two spans in the two directions. The RC slabs are 80 mm thick, with beam height and width equal to 180 and 100 mm, respectively. The columns have square cross-section with 150 mm side at the first floor, 130 mm at the second floor and 100 mm at the third floor. Details of geometrical properties and steel reinforcements for beams and columns are also reported in Figure 8.

The model and the additional masses (RC blocks rigidly joined to floor slabs) have been designed in order to have stresses in the model equal to those of a real building. Moreover, the real building has been designed with a limiting-damage criterion for very strong ground motions for Italy (peak acceleration equal to 0·35g). Beam-column nodes have been designed for low ductility levels and with the criterion of avoiding plastic hinge formation in columns. The model

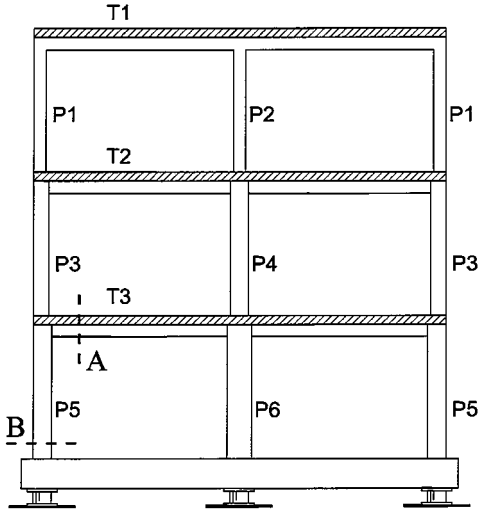

	J_{ci} (cm^4)	Steel Reinf.	Section
P1	1298	8ϕ6	
P2	3463	8ϕ6	
P3	5936	4ϕ8+4ϕ6	
T1	6851	(4+4)ϕ6	
T2	6851	(4+4)ϕ6	
T3	7107	(5+5)ϕ6	

Figure 8. 1/3-scale model of RC frame tested at Ismes Laboratory (Bergamo, Italy). J_{ci}: Inertia moment of the RC cross-section

was fixed at a metallic basement and placed over nine HDRB isolators with rubber height $h_g = 30$ mm, with hysteresis loops analogous to that reported in Figure 4. More details of the model and material properties are reported in Reference 5. The time scale for the model is $1/\sqrt{3}$ of that of the real structure.

The vibration period, in the linear range, of not isolated structure is equal to 0·17 s. The vibration period of isolated structure, considering for the isolators the secant stiffness with a shear strain equal to 25 per cent, is equal to 0·48 s (corresponding to 0·8 s for the real structure). Hence, only partial isolation effect can be expected, with stress level reaching the non-linear range in some cases (in usual design, natural periods of isolated structures are equal to 2 s or more).

The results reported by the authors in Reference 5 show good agreement between shaking-table experimental tests and numerical analyses for both displacements and accelerations. In order to verify the effectiveness of base-isolation system adopted, numerical simulations have been performed here, concerning conventional and base-isolated structures subject to two

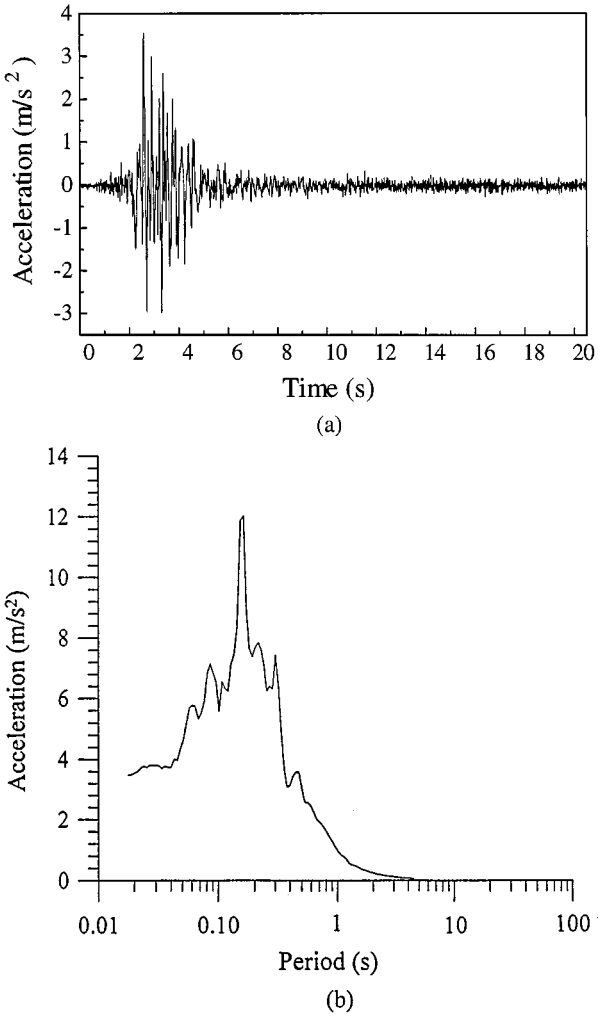

Figure 9. Tolmezzo earthquake: (a) accelerogram; and (b) corresponding response spectrum in the time scale of the model

different earthquakes whose ground motion accelerations have been recorded at Tolmezzo and Calitri, Italy (see Figures 9 and 10).

Tolmezzo earthquake is characterized by a very short duration (4–5 s in the model time scale), high acceleration peaks ($a_{max} = 3{\cdot}4$ m/s^2), and large values of response spectrum for short-period structures ($T < 0{\cdot}4$ s). Figure 11 shows the energy dissipated during hysteresis loops by the fixed-base RC structure and, for the isolated structure, by RC superstructure and isolators separately. In this case, the effectiveness of base-isolation system is evident, allowing for the reduction of dissipated energy (and consequent potential damage) up to 35 per cent. The hysteresis loops for beams and columns (sections denoted by 'A' and 'B' in Figure 8) are reported

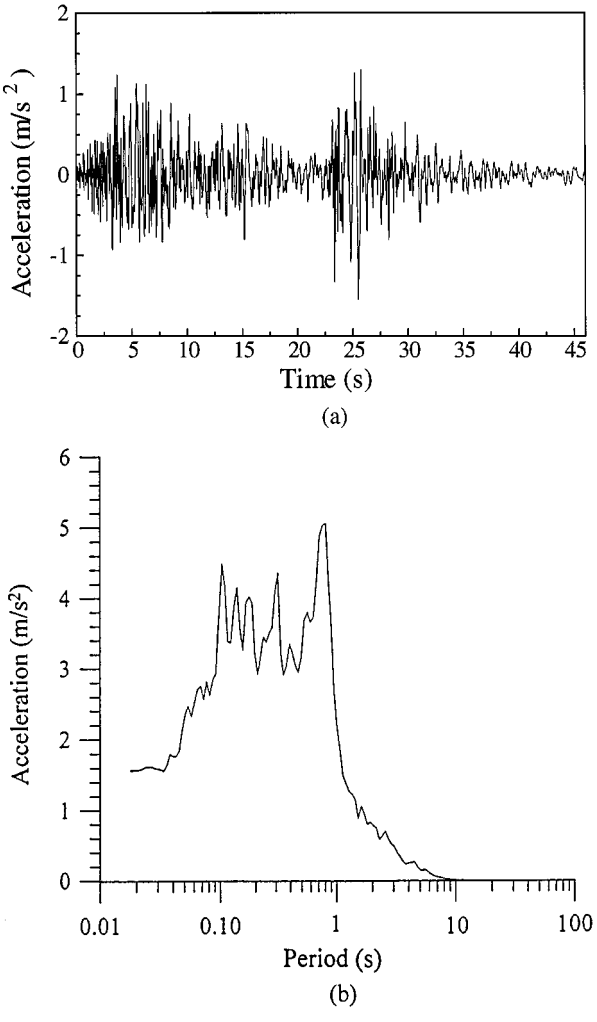

Figure 10. Calitri earthquake: (a) accelerogram; and (b) corresponding response spectrum (time scale of the model)

in Figures 12(a)–12(d), showing that base isolation allows for an effective damage protection especially of columns, exceeding only slightly the linear range.

In the second numerical simulations, the two structures are subject to Calitri earthquake ground motion (Figure 10), characterized by a very long duration (about 35 s) and lower accelerations with respect to the previous case ($a_{max} = 1{\cdot}2$ m/s^2). Nevertheless, the range of high energy containing frequencies is very wide, between 0·1 and 1 s. Figures 13–15 show the dissipated energy and power (energy per unit of time) by RC superstructure during hysteresis loops. The influence of HDRB stiffness, related to rubber layer height h_g, is also investigated.

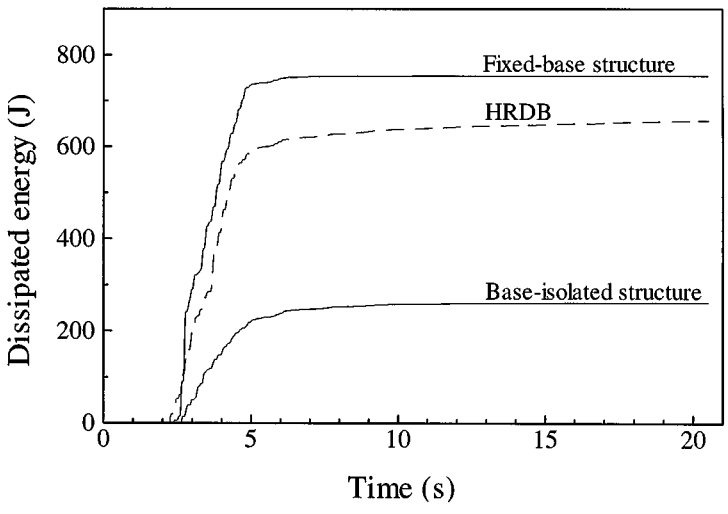

Figure 11. Tolmezzo earthquake: Dissipated energy due to inelastic deformations in conventional and base-isolated structures

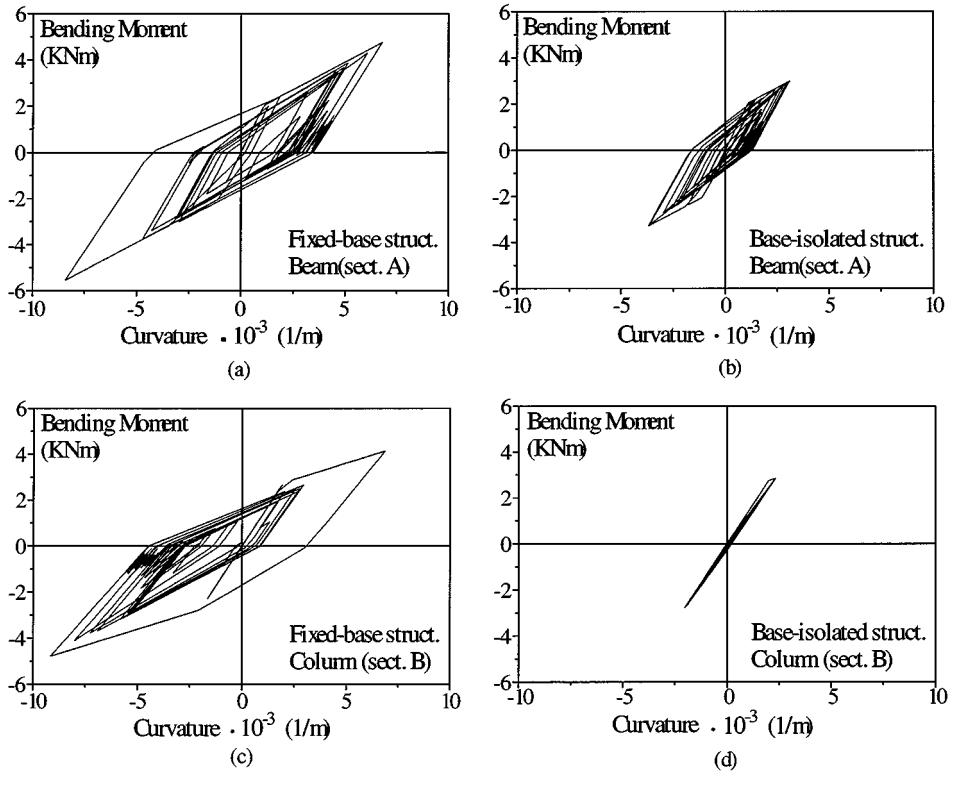

Figure 12. Tolmezzo earthquake: hysteresis loops for beam and column cross-sections: (a, c) conventional; and (b, d) base-isolated structure

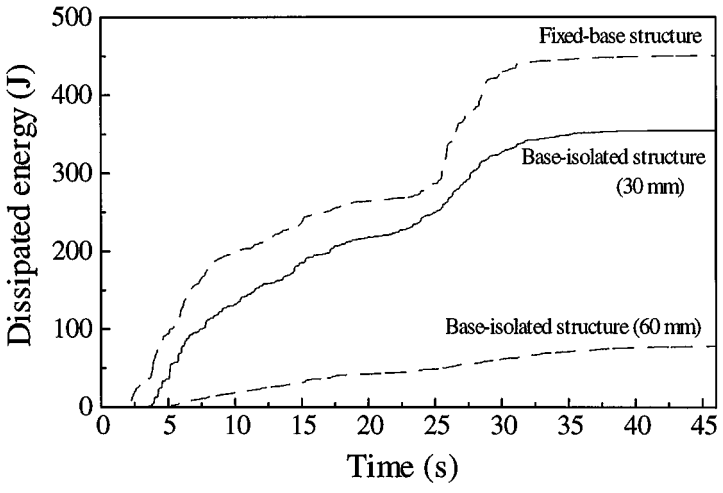

Figure 13. Calitri earthquake: dissipated energy due to inelastic deformations in conventional structure and base-isolated structures with 30 and 60 mm isolator heights

Figure 13 shows that the 30 mm isolator is effective only in the first seconds of excitation. A 21 per cent decrease only of dissipated energy with respect to fixed-base structure is obtained. A HDRB with 60 mm rubber height is much more effective, being able to drastically reduce damage in the superstructure during the whole earthquake excitation (83 per cent decrease of dissipated energy). Comparison of Figures 14(a) and 14(b) can draw the same conclusion. In Figure 15, dissipated energy for HDRBs with different rubber heights (up to 150 mm) is depicted. The figure confirms, as already outlined in previous papers[3], that an optimum range for the isolator stiffness exists, between 50 and 110 mm in the present case. In fact, adopting isolators with too low stiffness ($h_g > 110$ mm), resonance phenomena for low-frequency ground motions may occur with subsequent structural damage. This phenomenon is emphasized in Figure 14(c): hysteresis loops with consequent peaks of dissipated power are present almost during the whole earthquake excitation. In the time intervals 7–24 s and 29–38 s, base-isolated structure suffers even more inelastic deformations than conventional structure.

6. CONCLUSIONS

The seismic analysis of base-isolated RC structures has been performed. Hysteretic models for both RC members and HDRB isolators have been developed. For the isolators, a new model is proposed, which is able to reproduce the experimental hysteresis loops also in the large strain range. A block iterative Newton–Raphson algorithm has been developed for the numerical integration of dynamic equilibrium equations, based on the subdivision of the structure into superelement with master nodes at the extremities and internal local d.o.f.'s. The numerical algorithm has been used to verify, through some numerical examples, the effectiveness of base isolation in reducing potential structural damage. The roles played by earthquake duration and

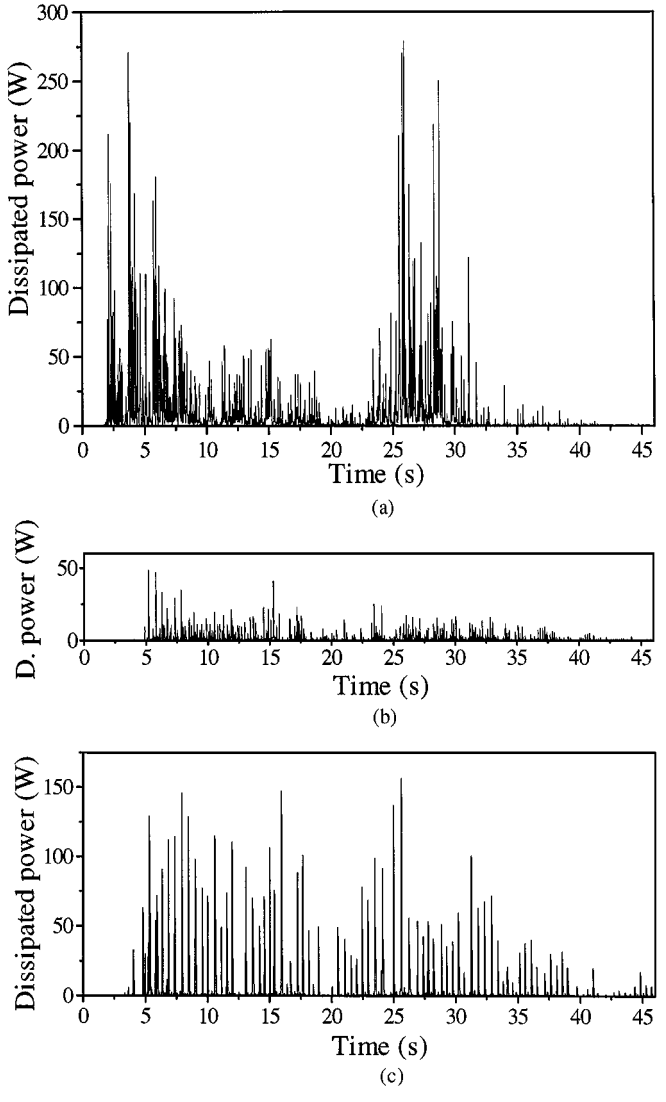

Figure 14. Calitri earthquake: dissipated power for: (a) fixed-base structure and for isolated structure with isolator heights; (b) 60 mm; and (c) 150 mm

frequency content have been discussed by comparing the effects of two different input motions, corresponding to Tolmezzo and Calitri (Italy) earthquakes. In the first case, (short duration and high-frequency content), base-isolation is always effective. On the contrary, in the second case (long-duration and low-frequency content) only a certain range of isolator stiffnesses appears to be effective. The present study represents the starting point for future extensive analyses on effectiveness of isolation for earthquake protection.

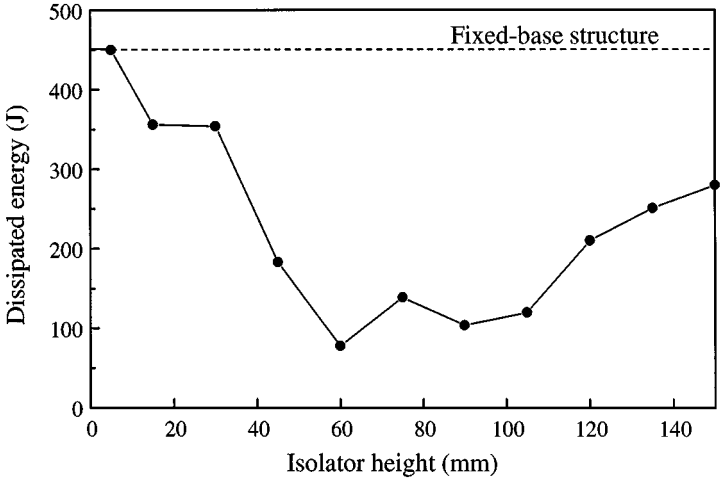

Figure 15. Calitri earthquake: dissipated energy in base-isolated structure with HDRB isolators having different rubber thicknesses. (- - -) Fixed-base structure

ACKNOWLEDGEMENT

The financial support of the (Italian) Ministry of University and Scientific and Technological Research (MURST – ex 60%) is gratefully acknowledged. The experimental tests on HDRBs were undertaken at Ismes Dynamic Laboratory (Bergamo, Italy) as a part of the joint research project "Technologies for the Earthquake Protection of Buildings" financed by the COSMES group.

REFERENCES

1. J. M. Kelly, 'Aseismic base-isolation: review and bibliography', *Soil Dyn. Earthquake Engng.* **8**, 202–216 (1986).
2. H. W. Shenton III and A. N. Lin, 'Relative performance of fixed-base and base-isolated concrete frames', *J. Struct. Engng.* ASCE **119**, 2952–2968 (1993).
3. J. A. Inaudi and J. M. Kelly, 'Optimum damping in linear isolation systems', *Earthquake Engng. Struct. Dyn.* **22**, 583–598 (1993).
4. H. C. Tsai and J. M. Kelly, 'Seismic response of heavily damped base-isolation systems', *Earthquake Engng. Struct. Dyn.* **22**, 633–645 (1993).
5. C. Ceccoli, C. Mazzotti and M. Savoia, 'Analytical and experimental seismic analysis of R. C. frame structures', in G. D. Manolis, D. E. Beskos, C. A. Brebbia (eds.), *Earthquake Resistant Engineering Structures*, Comput. Mech. Publications, Southampton, 1996, pp. 171–192.
6. Y. Chen and G. Ahmadi, 'Performance of a high damping rubber bearing base-isolation system for a shear beam structure', *Earthquake Engng. Struct. Dyn.* **23**, 729–744 (1994).
7. M. Kikuchi and I. D. Aiken, 'An analytical hysteresis model for elastomeric seismic isolation bearings', *Earthquake Engng. Struct. Dyn.* **26**, 215–231 (1997).
8. J. M. Kelly, *Earthquake-Resistant Design with Rubber*, Springer, London, 1993.
9. A. Feriani and F. Perotti, 'The formation of viscous damping matrices for the dynamic analysis of MDOF systems', *Earthquake Engng Struct. Dyn.* **25**, 689–709 (1996).
10. CEB, *RC Frames under Earthquake Loading – State of Art Report*, T. Telford Publications, Lausanne, Switzerland, 1996.
11. K. J. Mørk, 'Response analysis of reinforced concrete structures under seismic excitation', *Earthquake Engng. Struct. Dyn.* **23**, 33–48 (1994).

12. D. Miramontes, O. Merabet and J. M. Reynouard, 'Beam global model for the seismic analysis of RC frames, *Earthquake Engng Struct. Dyn.* **25**, 671–688 (1996).
13. Y. J. Park, A. M. Reinhorn and S. K. Kunnath, 'IDARC: inelastic damage analysis of reinforced concrete frame-shear wall structures', *Tech. Rep. NCEER-87-0008*, University of Buffalo, New York, 1987.
14. N. Makris, 'Rigidity-plasticity-viscosity: can electrorheological dampers protect base-isolated structures from near-source ground motions?', *Earthquake Engng. Struct. Dyn.* **26**, 571–591 (1997).
15. W. D. Iwan, 'Near-field considerations in specification of seismic design motions for structures', in G. Duma (ed.), *10th Europ. Conf. Earthquake Engng*., Balkema, Rotterdam, 1995, pp. 257–267.
16. W. D. Iwan and X. Chen, 'Important near-field ground motion data from the Landers earthquake', in G. Duma (ed.), *10th Europ. Conf. Earthquake Engng*., Balkema, Rotterdam, 229–234 (1995).
17. K. J. Mørk, 'Stochastic analysis of reinforced concrete frames under seismic excitation, *Soil Dyn. Earthquake Engng.* **11**, 145–161 (1992).
18. A. C. Costa and A. G. Costa, 'Hysteretic model for force-displacement relationships for seismic analysis of structures', Lab. Nat. de Engenh. Civil, Lisbon, 1987.
19. M. Saatcioglu, A. T. Derecho and W. G. Corley, 'Modelling hysteretic behavior of coupled walls for dynamic analysis', *Earthquake Engng. Struct. Dyn.* **11**, 711–726 (1983).
20. A. K. Chopra, *Dynamics of Structures — Theory and Applications to Earthquake Engineering*, Prentice-Hall, Englewood Cliffs, NJ, 1995.
21. CEB, *CEB-FIP Model Code 1990*, T. Telford Publications, Lausanne, Switzerland, 1990.
22. Y. J. Park and A. H. S. Ang, 'Mechanistic seismic damage model for reinforced concrete', *J. Struct. Engng.* ASCE **111**, 722–739 (1985).
23. K. J. Bathe and E. L. Wilson, *Numerical Methods on Finite Element Analysis*, Prentice-Hall, Englewood Cliffs, NJ, 1976.
24. A. H. Barbat, N. Molinares and R. Codina, 'Effectiveness of block iterative schemes in computing the seismic response of buildings with non-linear base-isolation' *Comput. Struct.* **58**, 133–141 (1996).
25. E. L. Wilson and J. Penzien, 'Evaluation of orthogonal damping matrices', *Int. J. Numer. Meth. Engng.* **4**, 5–10 (1972).
26. R.W. Clough and J. Penzien, *Dynamics of Structures*, McGraw-Hill, New York, 1975.
27. Y.J. Park, A.H.S. Ang and Y. K. Wen, 'Seismic damage analysis of reinforced concrete buildings', *J. Struct. Engng.* ASCE **111**, 740–757 (1985).
28. M. L. Wang and S.P. Shah, 'Reinforced concrete hysteresis model based on the damage concept', *Earthquake Engng. Struct. Dyn.* **15**, 993–1003 (1987).
29. E. Cosenza, G. Manfredi and R. Ramasco, 'The use of damage functionals in earthquake engineering: a comparison between different methods', *Earthquake Engng. Struct. Dyn.* **22**, 855–868 (1993).
30. Y. H. Chai, K. M. Romstad and S. M. Bird, 'Energy-based linear damage model for high-intensity seismic loading, *J. Struct. Engng.* ASCE **121**, 857–864 (1995).

